Dalton Transactions

ROYAL SOCIETY OF CHEMISTRY

PAPER

View Article Online
View Journal

Cite this: DOI: 10.1039/d6dt00689b

Evidence of aggregation-assisted antibacterial photodynamic activity against *S. aureus* and *E. coli* using amphiphilic Ru(II) polypyridyl complexes

Athanasios K. Sakellariou,[a] Sofia Alexandra Tsoni,[a] Despoina Varna,[a] Maria Nikopoulou,[b] Eleni Pavlidou,[c] Rigini Papi,[a] Sylvestre Bonnet[d] and Theodore Lazarides *[a]

Antimicrobial resistance represents a critical public health challenge, driving the search for therapeutic strategies that bypass conventional resistance mechanisms. Antimicrobial photodynamic therapy (aPDT) offers a promising alternative that is based on light-triggered non-specific oxidative damage. Herein, we report four new bis-heteroleptic Ru(II) complexes, with the general formula $[Ru(N–N)_2(N–NX)]Cl_2$, where N–N are the ancillary ligands, 2,2′-bipyridine (bpy) or 4,7-diphenyl-1,10-phenanthroline (DIP), and N–NX is a polyether-functionalized phenanthroline ligand. This design preserves the favourable photophysical characteristics of the $[Ru(bpy)_3]^{2+}$ core while enabling lipophilicity modulation. Dynamic light scattering and emission lifetime studies support that the complexes bearing the DIP ligand (**Ru-DIP-O3** and **Ru-DIP-O4**) self-assemble into nanoaggregates in aqueous media due to their amphiphilic nature, whereas their bpy analogues remain in their monomeric form. We propose a previously undescribed aggregate architecture in which the Ru(II) core is shielded within the hydrophobic interior, while the polyether chains remain solvent-exposed. Biological evaluation of the complexes against *S. aureus* strains reveals that **Ru-DIP-O3** and **Ru-DIP-O4** significantly inhibit bacterial growth, while the bpy derivatives exhibit negligible activity. Notably, **Ru-DIP-O4** demonstrates at least a 16-fold enhancement in the bacteriostatic rate upon irradiation relative to dark conditions. Scanning electron microscopy studies provide evidence of membrane disruption in irradiated bacteria treated with **Ru-DIP-O4**. We attribute the enhanced photodynamic activity of the DIP-based complexes to aggregation-driven interactions with the bacterial membrane. Collectively, these findings underscore the therapeutic potential of rationally designed Ru(II) complexes for photodynamic applications and highlight the roles of amphiphilicity and nanoscale self-assembly as key parameters for the design of next generation aPDT agents.

Received 23rd March 2026,
Accepted 28th April 2026

DOI: 10.1039/d6dt00689b

rsc.li/dalton

Introduction

The rapid escalation of antimicrobial resistance (AMR) poses a severe global health emergency.[1,2] This alarming situation is primarily driven by the widespread misuse of antibiotics, which has led bacteria to develop sophisticated survival strategies. These include drug efflux, enzymatic inactivation (*e.g.*, β-lactamases), and target site modification.[3–6] As the discovery of novel antibiotic scaffolds slows down, the gap between the emergence of resistance and the development of new therapeutics continues to widen.[7] This necessitates the development of non-conventional antibacterial strategies that bypass existing resistance pathways.[8]

Antimicrobial photodynamic therapy (aPDT) has emerged as a promising alternative, especially for localised infections in dentistry and dermatology.[9] In aPDT a photosensitiser (PS), administered as a prodrug at the infection site, is activated upon irradiation with light in the visible or near-infrared region, subsequently leading to the generation of cytotoxic reactive oxygen species (ROS). Distinct from the specific "key-and-lock" mechanism of traditional antibiotics, aPDT induces rapid, non-specific oxidative stress on multiple bacterial components, including cell membranes and nucleic acids.[10] It is thus believed that the multi-target, non-pathway-specific nature of aPDT can make the development of bacterial resis-

[a]*Department of Chemistry, Aristotle University of Thessaloniki, 54124 Thessaloniki, Greece. E-mail: tlazarides@chem.auth.gr*
[b]*Department of Geology, Aristotle University of Thessaloniki, 54124 Thessaloniki, Greece*
[c]*Department of Physics, Aristotle University of Thessaloniki, 54124 Thessaloniki, Greece*
[d]*Leiden Institute of Chemistry, Leiden University, Einsteinweg 55, 2333CC Leiden, The Netherlands*

tance within a reasonable therapeutic timeframe less likely than with conventional antibiotics. However, bacteria may develop adaptive responses towards aPDT, for instance, through upregulation of efflux pumps and/or activation of their natural ROS scavenging systems.[11] It is therefore important to view aPDT as one more tool in a multifaceted strategy against antimicrobial resistance.[12]

Organic dyes (*e.g.*, porphyrins, phthalocyanines) have been traditional cornerstones of aPDT research. However many organic photosensitisers face challenges like photobleaching, aggregation-induced quenching, and limited modular tunability.[13,14] Transition metal complexes have recently attracted attention as promising alternatives owing to their improved photostability and tunable photophysical properties.[15] Ru(II) polypyridyl complexes are particularly attractive in this context as they possess a long-lived triplet metal-to-ligand charge transfer (^{3}MLCT) excited state which forms readily after rapid intersystem crossing of the initially populated singlet ^{1}MLCT state.[16] The relatively long lifetime of the ^{3}MLCT excited state facilitates efficient singlet oxygen ($^1O_2$) generation upon its interaction with molecular oxygen *via* energy transfer (type II PDT mechanism, $\mathbf{[Ru(bpy)_3]^{2+}}$; Φ_Δ = 0.57 in MeCN).[17] Alternatively, the ^{3}MLCT state can participate in the production of other reactive oxygen species (ROS), including superoxide or hydroxyl radicals, *via* electron transfer processes (type I PDT mechanism).[18] Additionally, Ru(II) complexes with polypyridyl ligands featuring substituents with extended conjugation, such as oligothiophene groups,[19] polyaromatic units[20] or dyes,[21] can facilitate PDT through triplet intraligand (^{3}IL/^{3}ILCT) excited states. However, despite their favourable photophysical properties, the antimicrobial performance of Ru(II) photosensitisers is often dictated by their ability to interact with or penetrate the bacterial envelope, rather than their intrinsic excited-state properties alone.[22]

Therefore, recent research has focused on ligand design strategies aimed at enhancing bacterial association and uptake while limiting dark toxicity and enhancing desired phototoxicity.[23] Representative approaches include modulation of electrical charge and lipophilicity, bioconjugation with membrane-targeting or biologically relevant motifs, and incorporation of ligands capable of directing the photosensitiser toward specific intracellular targets.[24–27]

In this context, Zhang and co-workers reported a Ru(II) complex functionalised with a myristic acid moiety, thus promoting membrane targeting through lipophilic interactions.[28] Angeles-Boza *et al.* demonstrated enhanced antimicrobial activity by conjugating the DNA-targeting peptide "buforin II" to a Ru(II) photosensitiser.[29] In a complementary approach, Hess and co-workers developed a Ru(II) complex capable of photodynamically degrading the β-lactamase NDM-1, thereby directly targeting a key resistance mechanism.[30] In addition, nanoparticle-based delivery strategies have also been explored to improve PS performance.[31,32] For example, Sun and co-workers reported a $[Ru(bpy)_2dppz]^{2+}$ based nanomaterial modified with outer layers that can adhere to bacterial membranes.[33] Also, the Gasser and Karges groups have reported several ruthenium complexes encapsulated with polymers which improve the pharmacological activity of the PS.[34–36]

Overall, the interaction of photosensitisers with bacterial cells is strongly influenced by their physicochemical properties.[37] While increased lipophilicity can enhance membrane association and permeation, excessively hydrophobic molecules often exhibit aggregation, reduced aqueous stability, or elevated dark toxicity, ultimately hindering drug performance.[38] In contrast, amphiphilic architectures, in which hydrophilic and hydrophobic domains coexist, can promote effective interactions with bacterial membranes while mitigating the drawbacks associated with excessive lipophilicity. The optimal balance of these properties is further influenced by the architecture of the bacterial cell envelope. Gram-positive bacteria, characterised by a thick yet relatively permeable peptidoglycan-rich cell wall, are generally more accessible to amphiphilic photosensitisers. On the other hand, Gram-negative bacteria possess an additional outer membrane enriched in lipopolysaccharides that restricts diffusion and complicates photosensitiser uptake.[39,40] Therefore, rational modulation of amphiphilicity represents a key design principle in the development of Ru(II) photosensitisers for selective and efficient antimicrobial photodynamic therapy.

Previous studies by De Cola and co-workers have shown that Ru(II) polypyridyl complexes bearing long aliphatic chains can self-assemble into micelle-like aggregates in aqueous media. In these aggregates, the $\mathbf{[Ru(bpy)_3]^{2+}}$ core functions as a polar headgroup positioned at the aggregate periphery.[41] More recently, Keyes and co-workers investigated the cellular uptake of related highly lipophilic Ru(II) polypyridine complexes and showed that their self-assembly into nanoscale vesicles can enhance cell membrane permeability.[42–44] Self-delivering amphiphilic drugs are constructed by covalently attaching hydrophilic and/or hydrophobic moieties to a drug molecule. This enables the resulting conjugate to self-assemble into nanoscale aggregates, facilitating the crossing of biological barriers without the need for a separate nanocarrier. Such assemblies are distinguished by their fixed and intrinsically high drug loadings, in contrast to conventional nanoparticle-based delivery systems, in which the active agent typically constitutes a small fraction of the total mass. Moreover, eliminating the use of a separate nanocarrier can reduce carrier-related toxicity and simplify formulation.[45,46] Bacteria do not typically have the ability to internalize nanoscale assemblies by endocytosis as is observed in eucaryotic cells. However, nanoassemblies comprising cationic amphiphilic drugs interact strongly with the anionic bacterial envelope. Thus, the assemblies localize and are retained at the cell surface, where partial disassembly can release active molecules which subsequently partition into the membrane.[47–49]

In this work, we report four new Ru(II) polypyridyl complexes bearing polyether-functionalised ligands, designed to investigate whether their finely tuned amphiphilicity and ability to self-assemble into nano-dimensional aggregates can enhance aPDT efficacy. Our objective is to explore an alternative and previously unexplored approach for photosensitisers based on the $\mathbf{[Ru(bpy)_3]^{2+}}$ core, in which hydrophilic polyether chains form the

outer shell of the assembly, while the photoactive Ru(II) core is located in the interior of the aggregate (Fig. 1). In contrast to previously reported assemblies, this alternative organisation enables the complexes to function as self-assembled nanocarriers while simultaneously maintaining favourable overall amphiphilicity that is desired for facilitating interactions with bacterial membranes. Micelles featuring Ru(II) polypyridyl centres functionalised with long poly(ethylene glycol) (PEG) chains attached to a poly(methyl methacrylate) (PMMA) backbone[50] or incorporated within a block copolymer[51] have been previously described. However, in these cases, the interior of the micelle is formed by the hydrophobic part of the respective polymer, while the Ru(II) units are permanently attached to the polymer scaffold. To probe the role of amphiphilicity in our complexes, the polyether-functionalised ligands were combined with either 2,2′-bipyridine (bpy) or the more lipophilic 4,7-diphenyl-1,10-phenanthroline (DIP), thus allowing a direct comparison between Ru(II) complexes of relatively uniform hydrophilicity (bpy complexes) and those designed to display hydrophilic–hydrophobic asymmetry (DIP complexes). $[Ru(DIP)_2phen]Cl_2$ was utilized to further explore the contribution of the polyether chains in the DIP-containing architecture.

Results and discussion

Synthesis and characterisation

We synthesized our polyether-functionalized phenanthroline ligands *via* a nucleophilic substitution between 5-hydroxy-1,10-phenanthroline [**2**] and the corresponding halogenated polyether chain (Scheme 1). This approach afforded two new phenanthroline ligands, **L-O3** and **L-O4**, with each bearing polyether substituents of differing chain lengths in their 5-positions, one with three oxygen atoms and the other with four oxygen atoms respectively. These ligands were designed to enhance hydrophilicity in aqueous environments by facilitating hydrogen-bonding interactions. Subsequently, they were coordinated to two distinct Ru(II) precursor complexes, allowing for systematic modulation of lipophilicity by varying the ancillary ligands. Characterisation of the ligands **L-O3** and **L-O4** was performed *via* ^{1}H-NMR spectroscopy (Fig. S2 and S3) and electrospray ionization mass spectrometry (ESI-MS, Fig. S4 and S5).

The ligands **L-O3** and **L-O4** were refluxed with either *cis*-$[Ru(bpy)_2Cl_2]$ or *cis*-$[Ru(DIP)_2Cl_2]$ in a 1 : 1 EtOH/H_2O mixture overnight, affording four final complexes: $[Ru(bpy)_2$(**L-O3**$)]Cl_2$ (**Ru-bpy-O3**), $[Ru(bpy)_2$(**L-O4**$)]Cl_2$ (**Ru-bpy-O4**), $[Ru(DIP)_2$(**L-O3**$)]Cl_2$ (**Ru-DIP-O3**), and $[Ru(DIP)_2$(**L-O4**$)]Cl_2$ (**Ru-DIP-O4**) (Scheme 1). All complexes were purified *via* silica gel column chromatography using a $MeCN/KNO_{3(aq)}$ (0.05 M) gradient as the eluent and subsequently converted to their chloride salts *via* ion-exchange chromatography to improve aqueous solubility and biocompatibility. In addition, $[Ru(DIP)_2phen]Cl_2$, which was synthesized according to literature procedures,[52] served as a control compound. All new complexes were characterised *via* both one-dimensional and two-dimensional NMR (^{1}H, ^{13}C APT, ^{1}H–^{1}H COSY and ^{1}H–^{13}C HSQC, Fig. S8–24),

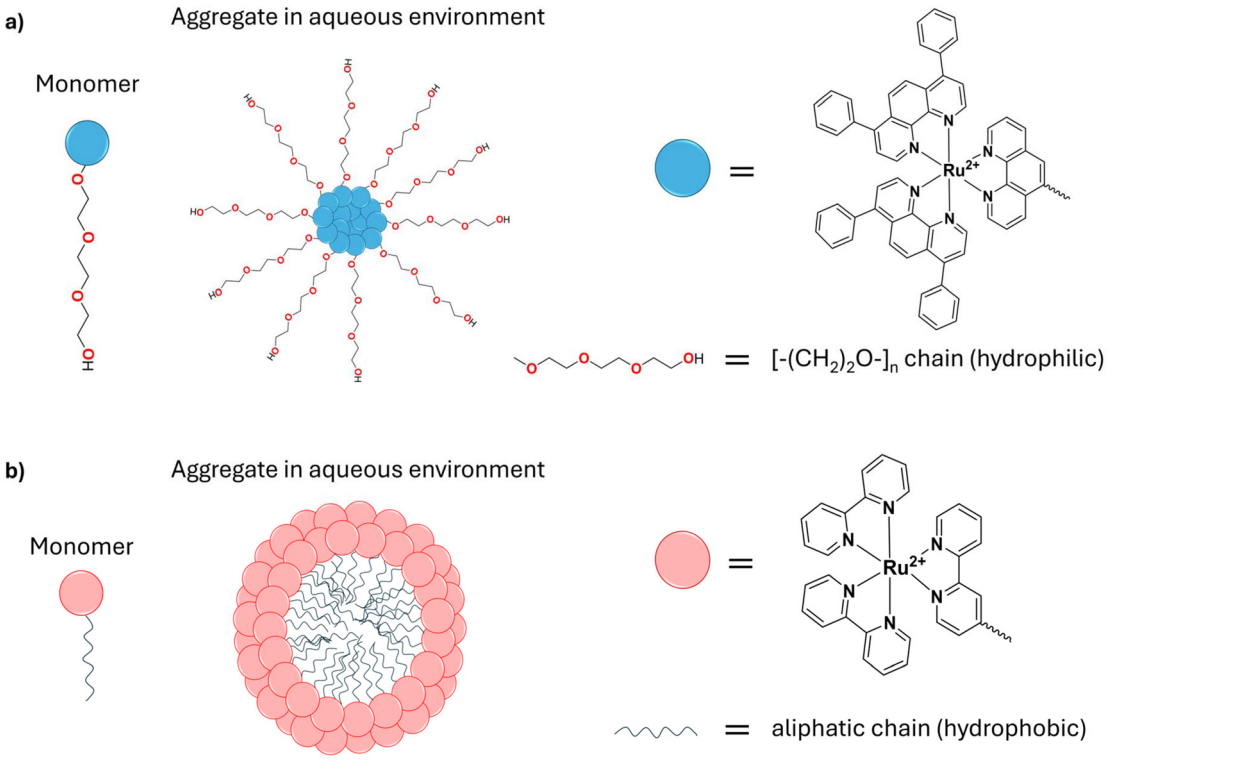

Fig. 1 Graphical representation of the different aggregation modes between (a) our proposed structure and (b) previously reported Ru(II) complexes.

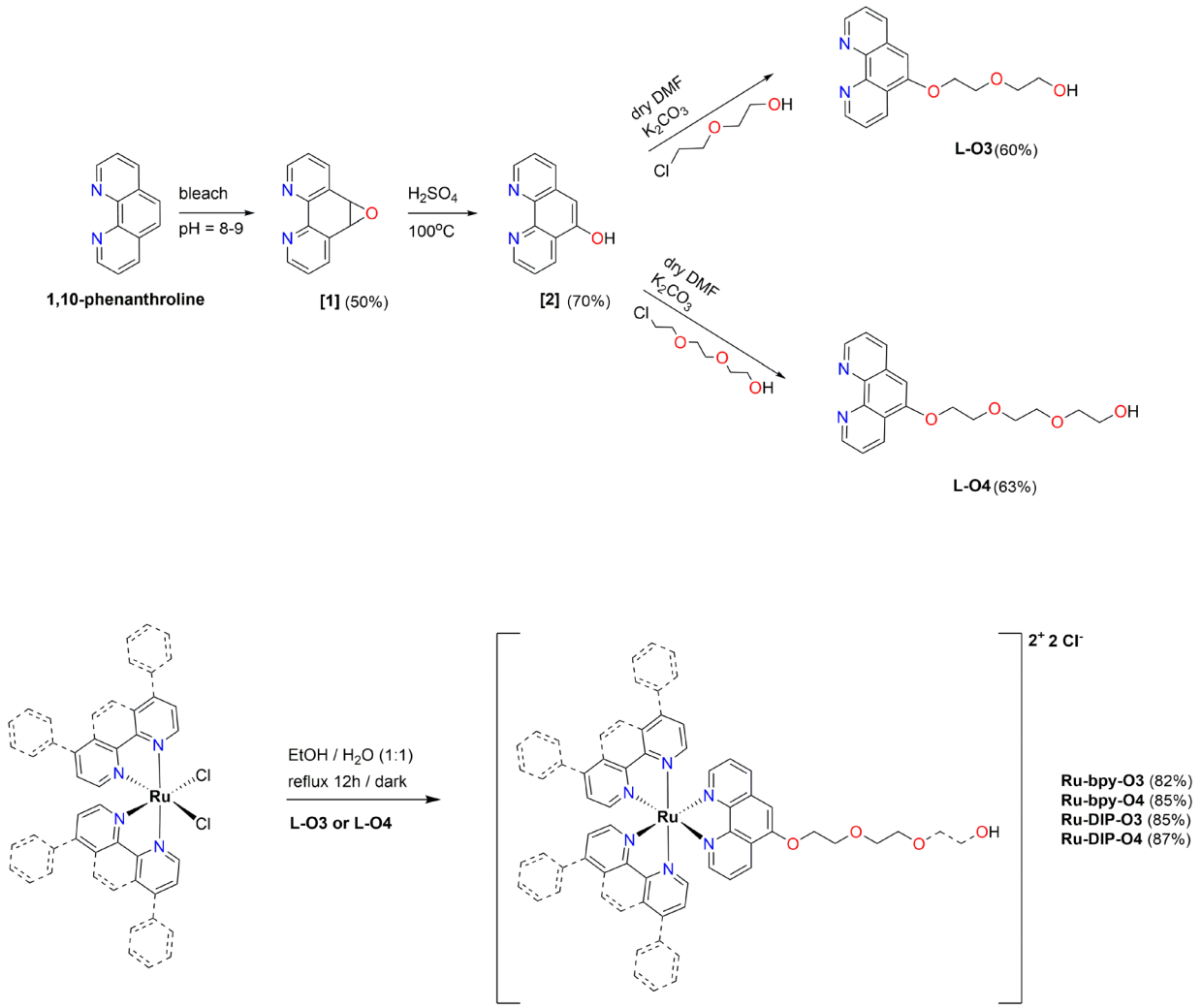

Scheme 1 General synthetic route for the studied compounds.

as well as high-resolution mass spectrometry (HRMS, Fig. S25–28). The use of 2D NMR techniques was required due to the structural asymmetry introduced by the ligands **L-O3** and **L-O4**. The purity of the complexes was confirmed *via* liquid chromatography–mass spectrometry (LC-MS, Fig. S29–S32).

Lipophilicity assessment

As discussed above, the lipophilicity of a compound is of crucial importance when assessing its potential interaction with the microbial cell envelope. Thus, the partition coefficient ($\log P_{o/w}$) between octanol and water of each new complex was determined (Fig. 2) *via* the shake-flask method.[53] **Ru-bpy-O3** and **Ru-bpy-O4**, which feature bpy as an ancillary ligand, display high hydrophilicity as the complexes were not detectable *via* UV-vis spectroscopy in the octanol phase. It was therefore assumed that less than 0.1% of the initial amount of the complexes was distributed to the octanol phase and a tentative $\log P_{o/w}$ value of ≤−3 was assigned.[54] Meanwhile, **Ru-DIP-O3** and **Ru-DIP-O4**, which feature the more lipophilic DIP as an

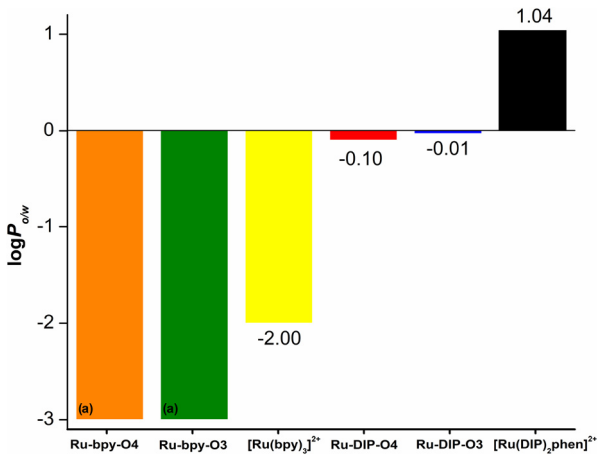

Fig. 2 Octanol–water partition coefficients ($\log P_{o/w}$) of the studied complexes as their chloride salts, and $[Ru(DIP)_2phen]Cl_2$ was used for comparison. The "(a)" in the figure indicates that the distribution of these complexes in octanol was too low to be determined and was assumed as <0.1%.

ancillary ligand, display an amphiphilic character as their log $P_{o/w}$ values were found to be close to zero (−0.10 and −0.01 respectively). It is worth noting that **Ru-DIP-04**, which features a polyether chain extended by one more –$(CH_2)_2O$– group compared to **Ru-DIP-O3**, is more hydrophilic. $[Ru(DIP)_2phen]Cl_2$ has a log $P_{o/w}$ value of 1.04, verifying that the absence of a polyether chain makes the complex clearly lipophilic.

Aggregation studies

It is well established that Ru(II) polypyridyl complexes exhibiting a sufficient degree of amphiphilicity can self-assemble into aggregates in aqueous media.[55] However, in our complexes the amphiphilic architecture differs fundamentally from previously reported systems, where the cationic Ru(II) "headgroup" is linked to an extended hydrophobic ligand "tail", thus promoting micelle-like organisation with the metal centre exposed to the aqueous environment. In contrast, in our system the π-extended lipophilic DIP ligands attached to the Ru(II) core can be considered as the hydrophobic domain, while the appended polyether chains constitute the hydrophilic segment. This polarity distribution within the complex is expected to lead to an alternative aggregation mode in water, where the DIP ligands are organised in the interior of the aggregate and the flexible polyether chains are oriented toward the aqueous phase, thereby shielding the Ru(II) core in the middle of the proposed structure.

Dynamic light scattering (DLS) measurements were performed in Tris-HCl buffer (0.05 M, pH 7.4) over a concentration range of 6–50 μM, reflecting that used in the antibacterial assays. Clear nanoaggregate formation was observed for **Ru-DIP-O3** and **Ru-DIP-O4**, which displayed relatively narrow particle size distributions (Fig. 3), with average hydrodynamic diameters of 259 and 287 nm, respectively (Table S1). **Ru-DIP-O4** retained well-defined distributions across the examined concentration range, whereas **Ru-DIP-O3** stopped displaying signs of aggregation below 12.5 μM. The relatively large hydrodynamic diameters further suggest the formation of higher-order multivesicular or bilayer-type assemblies rather than simple micelles.[56,57] In contrast, the bpy-containing analogues showed no detectable aggregation under identical conditions.

For comparison, the lipophilic control complex $[Ru(DIP)_2phen]Cl_2$ was also examined. Although aggregation was detected in aqueous buffer at 50 μM, the particle size distribution was broader and more polydisperse (hydrodynamic diameter = 416 nm, polydispersity index = 0.32; Table S1), with a substantially weaker scattering signal. At concentrations below 50 μM, no signs of aggregation were observed. Collectively, these results indicate weaker intermolecular interactions and less dynamically stable assemblies relative to **Ru-DIP-O3** and **Ru-DIP-O4**,[58] supporting the role of polyether functionalisation in promoting a distinct supramolecular architecture.

To assess aggregation under biologically relevant conditions, DLS measurements were additionally performed in M9 bacterial growth medium (50 μM; Fig. S33). Both **Ru-DIP-O3** and **Ru-DIP-O4** formed aggregates (average hydrodynamic diameters of 271 and 341 nm, respectively; Table S1), demonstrating that self-assembly persists in this more complex environment and is primarily driven by aqueous conditions rather than specific buffer components.[59]

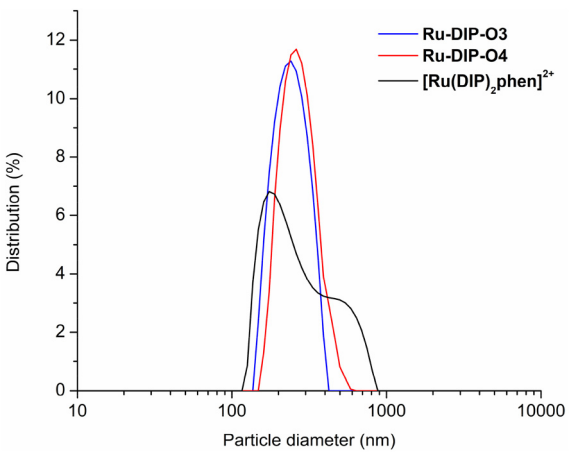

Fig. 3 DLS analysis of the studied compounds (50 μM) in Tris–HCl buffer (0.05 M, pH = 7.4).

Photophysical characterisation

The photophysical properties of our complexes were studied in air-equilibrated MeCN and Tris–HCl aqueous buffer (0.05 M, pH = 7.4) at 298 K and in a frozen glass matrix (EtOH/MeOH, 4 : 1 v/v) at 77 K (Table 1). Specifically, as expected for **$[Ru(bpy)_3]^{2+}$** analogues, all complexes display strong absorption bands at *ca.* 250–280 nm, attributed to the fully allowed π–π* transitions of the polypyridyl ligands, and characteristic lower intensity bands in the region of 400–500 nm attributed to spin-allowed metal-to-ligand charge transfer (^{1}MLCT) transitions (Fig. 4a).[60] Complexes bearing the DIP ancillary ligands exhibit larger molar absorption coefficients than their bpy counterparts (Table 1), which can be attributed to the more extended π-conjugation of the DIP ligand, resulting in enhanced light-harvesting efficiency.[61]

Upon excitation at 450 nm under ambient conditions, all complexes exhibit an emission band, peaking at approximately 630 nm in Tris–HCl buffer and at approximately 620 nm in MeCN, corresponding to the radiative deactivation of a triplet metal-to-ligand charge transfer (^{3}MLCT) state, as expected for **$[Ru(bpy)_3]^{2+}$** based systems (Table 1). The slight red-shift noted in Tris–HCl buffer is attributed to stronger stabilisation of the charge transfer state in aqueous environments.[62] In EtOH/MeOH 4 : 1 glass at 77 K, the emission bands become vibronically resolved, revealing distinct fine structure, with peak maxima at 590 nm (2.10 eV) for DIP-containing complexes and 575 nm (2.15 eV) for bpy-containing complexes, corresponding to the E_{0-0} transitions (Fig. S35 and Table 1). The red-shifted emission observed for DIP-containing complexes arises from stabilisation of the ^{3}MLCT excited state due to the lower-lying π* orbitals of the DIP ligand.[63]

Due to the aforementioned stabilisation of the charge transfer state, as well as the lower concentration of dissolved mole-

Table 1 Selected steady-state photophysical data of the studied complexes and $[Ru(bpy)_3]^{2+}$

Compound	Medium	λ_{abs} (nm)	ε (M^{-1} cm^{-1})	λ_{em} (nm)	Φ (%)
Ru-bpy-O3	MeCN	451	1.6×10^4	616	1.7
	Tris–HCl	455	1.5×10^4	628	4.7
	Glass (77 K)	—	—	575 (max), 620	—
Ru-bpy-O4	MeCN	451	1.6×10^4	618	1.8
	Tris–HCl	452	1.5×10^4	625	4.7
	Glass (77 K)	—	—	575 (max), 620	—
Ru-DIP-O3	MeCN	460	3.0×10^4	624	1.3
	Tris–HCl	461	2.9×10^4	630	4.8
	Glass (77 K)	—	—	590 (max), 635	—
Ru-DIP-O4	MeCN	456	2.9×10^4	619	1.2
	Tris–HCl	457	2.8×10^4	630	5.0
	Glass (77 K)	—	—	590 (max), 635	—
$[Ru(bpy)_3]^{2+}$	MeCN	450	1.3×10^4	611	1.6 [64]
	H_2O	453	1.5×10^4	625	4.0 [65]
$[Ru(DIP)_2phen]^{2+}$	MeCN	452	2.8×10^4	620	1.3
	Tris–HCl	458	2.8×10^4	629	3.7

cular oxygen in aqueous solutions (which is the prime quencher of the ^{3}MLCT excited state) compared to MeCN, it is expected that longer emission lifetimes will be observed in aqueous environments. This is already confirmed in the literature as $[Ru(bpy)_3]^{2+}$ shows an emission lifetime of *ca*. 170 ns in MeCN and *ca.* 360 ns in water (both air-equilibrated).[64]

We performed emission lifetime measurements (Fig. 4b and Fig. S38–41) in MeCN and two different aqueous media: Tris–HCl buffer (0.05 M, pH = 7.4) and M9 bacterial growth medium (50 μM). Measurements in MeCN in comparison with aqueous conditions aim to explore the behaviour of the complexes in different solvents (organic *vs.* aqueous environment).

M9 bacterial growth medium was utilised in addition to Tris–HCl aqueous buffer to assess whether our complexes exhibit the same photophysical behaviour under the conditions of the antibacterial assays (*vide infra*). In agreement with previous observations, the complexes **Ru-bpy-O3** and **Ru-bpy-O4** display emission lifetimes of approximately 140 ns in MeCN and 380 ns in both aqueous media (Table 2). However, the picture is markedly different for the DIP-containing complexes, as they display biexponential decays comprising a major component with a strongly enhanced emission lifetime and a minor component with a shorter lifetime (Fig. 4b and Table 2). Indicatively, the decay of **Ru-DIP-O4** in M9 is ideally described by a 369 ns component (6.3%) and a longer 820 ns component (93.7%).

The presence of a predominant long-lived emission component in the order of 800 ns indicates that there is an additional factor, beyond solvent reorganisation effects, enhancing the emission lifetimes of our DIP derivatives.[66] We propose that the aggregation of the DIP complexes in aqueous media (*vide supra*) results in their structural rigidification, thereby suppressing their non-radiative deactivation pathways.[41,66] Therefore, we assign the shorter emission lifetime to the complexes in their monomeric form, while the longer lifetime is attributed to the Ru(II) chromophores within the aggregates. To provide further support for this hypothesis, we performed an additional experiment where 100 μL aliquots of a 50 μM solution of **Ru-DIP-O4** in MeCN were added to an equimolar solution of the complex in Tris–HCl buffer, while recording the emission decay of the resulting mixture after each addition. When the volume fraction of MeCN in Tris–HCl buffer reached 20%, we observed a sharp drop in emission lifetime from 790 ns to 410 ns, indicating that at this MeCN content the aggregates break and the emission corresponds predominantly to monomeric species (Fig. S43). This type of aggregation-induced emission lifetime enhancement has been previously observed in Ru(II) polypyridyl derivatives which self-assemble into aggregates.[41,66,67] However, it is important to mention that the close proximity between chromophores

Table 2 Emission lifetimes of the studied complexes in various media

Compound	Medium	τ (ns)	χ^2
Ru-bpy-O3	MeCN	143	1.02
	Tris–HCl	377	1.08
	M9	391	1.04
	Glass (77 K)	8693	1.03
Ru-bpy-O4	MeCN	143	1.06
	Tris–HCl	388	1.08
	M9	383	1.03
	Glass (77 K)	8477	1.09
Ru-DIP-O3	MeCN	170	1.00
	Tris–HCl	τ_1 = 215 (4.3%) τ_2 = 823 (95.7%)	1.05
	M9	τ_1 = 479 (16.2%) τ_2 = 892 (83.8%)	0.99
	Glass (77 K)	τ_1 = 5209 τ_2 = 11 287	1.13
Ru-DIP-O4	MeCN	176	0.93
	Tris–HCl	τ_1 = 285 (1.6%) τ_2 = 764 (98.4%)	1.03
	M9	τ_1 = 369 (6.3%) τ_2 = 820 (93.7%)	1.08
	Glass (77 K)	12 480	1.02
$[Ru(bpy)_3]^{2+}$	MeCN	156	1.02
	Tris–HCl	329	1.02
	M9	371	1.17
$[Ru(DIP)_2phen]^{2+}$	MeCN	170	1.09
	Tris–HCl	715	1.07
	M9	690	1.18

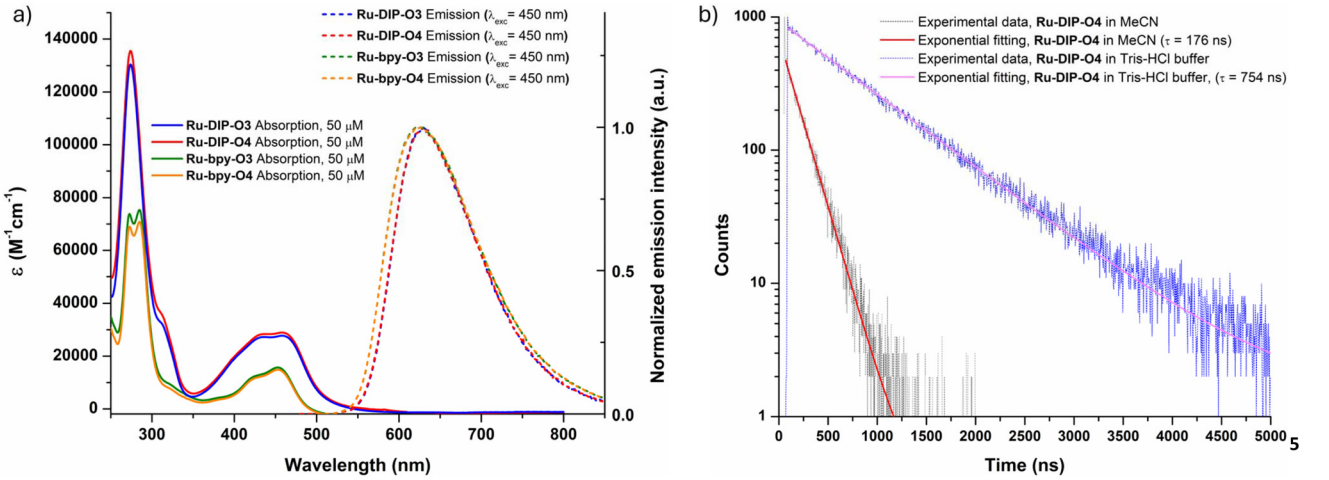

Fig. 4 Photophysical properties of the studied complexes. (a) Absorption (solid lines) and emission (dashed lines) spectra of the complexes (50 μM) in Tris–HCl buffer. (b) Experimental decay data and exponential fitting of **Ru-DIP-O4** in MeCN and Tris–HCl buffer.

within such an assembly can also cause emission quenching through interchromophoric energy transfer. Indeed, this was observed by Hammarström and co-workers who studied the incorporation of $[Ru(bpy)_3]^{2+}$ complexes functionalized with lipophilic tails on the surface of 1,2-dimyristoyl-*sn-glycero*-3-phosphocholine (DMPC) liposomes. Biexponential emission decays were observed with an increasing contribution of a short lifetime component as the local concentration of the Ru(II) chromophores was increased.[68] This suggests that in multichromophoric assemblies, two competing effects are at play: chromophore rigidification leading to emission enhancement and self-quenching. The dominance of one effect over the other depends on the specific conditions and characteristics of each system.

ROS generation studies

Ru(II) polypyridyl complexes possess a triplet excited state capable of interacting with molecular oxygen or other molecules in the photosensitiser's vicinity, thereby generating significant amounts of $^1O_2$ or ROS. The majority of these complexes operate predominantly as type II photosensitisers.[16] Therefore, direct measurements of $^1O_2$ photogeneration upon excitation of isoabsorbing (A = 0.1) solutions of our compounds at 450 nm in MeCN were performed by monitoring its characteristic phosphorescence signal at 1270 nm.[69] As seen in Fig. 5a, under the conditions described above, all the studied compounds give clear $^1O_2$ emission signals of similar intensities, indicating that they are efficient type II photosensitisers. Direct measurements were performed in MeCN due to the strongly increased intensity of $^1O_2$ phosphorescence in this medium compared to water.[53,54]

However, as our DIP-containing complexes exhibit distinct behaviour in aqueous media, namely aggregation and prolonged emission lifetimes, and since the antibacterial assays are also conducted under aqueous conditions, it is of interest to evaluate the ability of these complexes to photo-generate $^1O_2$ and other ROS in water. To this end, we performed indirect ROS generation experiments with the use of two probes: 9,10-anthracenediyl-bis(methylene)dimalonic acid (ABDA) and dihydrorhodamine-123 (DHR-123).

ABDA was selected due to its high selectivity toward $^1O_2$.[70] Upon reaction with $^1O_2$, ABDA undergoes irreversible endoperoxidation, resulting in a progressive decrease of its characteristic absorption band at 380 nm (Fig. 5b).[71] In contrast, DHR-123 serves as a generic probe for type I ROS. DHR-123 is oxidized by species such as superoxide and peroxide anions to form highly fluorescent (528 nm) rhodamine-123 (Fig. 5c).[72] For each complex, the decrease in ABDA absorbance and the increase in DHR-123 fluorescence at the selected wavelengths were plotted against time, and the initial rates were obtained from linear fits to these time courses and used as the relative assay scores (Fig. S44–S48). Our results demonstrate that all investigated complexes possess effective photosensitising activity, as both direct and indirect measurements reveal photogenerated levels of ROS comparable to those obtained for the reference photosensitiser $[Ru(bpy)_3]^{2+}$ (Fig. 5d–f). This observation indicates that functionalisation of the ligands does not compromise the intrinsic photochemical behaviour of the Ru(II) polypyridyl core, in line with expectations.

Notably, when examined under aqueous conditions, the DIP-containing complexes display a moderately enhanced response in the ABDA assay relative to their bpy analogues (Fig. 5e). Given that ABDA selectively reports on $^1O_2$ production, this observation suggests that type II photosensitisation is more effective for these derivatives in water. This behaviour is consistent with the observed aggregation behaviour of the DIP-containing complexes in aqueous media, which is accompanied by extended emission lifetimes. While aggregation is often associated with excited-state quenching, in this case it does not appear to suppress $^1O_2$ generation and may instead favour type II reactivity under these conditions.

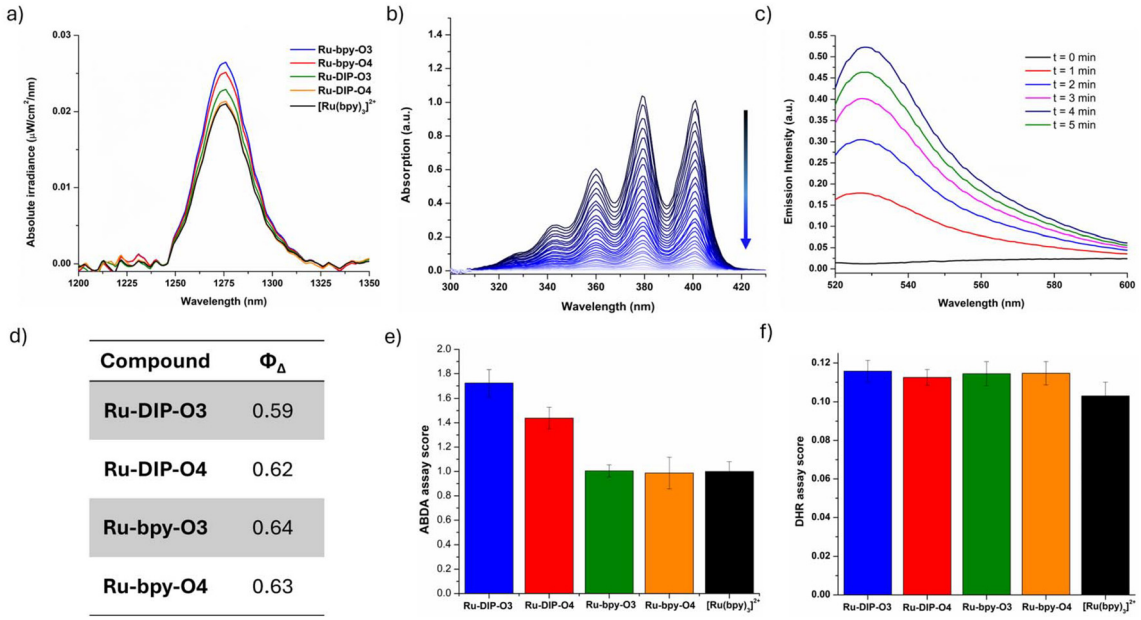

Compound	Φ_Δ
Ru-DIP-O3	0.59
Ru-DIP-O4	0.62
Ru-bpy-O3	0.64
Ru-bpy-O4	0.63

Fig. 5 Photoinduced ROS generation assessment. (a) Emission spectra of photogenerated $^1O_2$ upon irradiation of each compound at 450 nm in MeCN, (b) absorption spectra of ABDA upon irradiation of **Ru-DIP-O4** at 450 nm in PBS, (c) emission spectra of DHR-123 upon irradiation of **Ru-DIP-O4** at 450 nm in PBS, (d) table of $^1O_2$ generation quantum yields calculated from the direct method in MeCN, (e) ABDA assay scores for all compounds and (f) DHR-123 assay scores for all compounds.

Finally, to ensure stability upon irradiation under biologically relevant conditions, all complexes were irradiated (450 nm) in aqueous media at physiological temperature (37 °C) and monitored simultaneously using UV-vis spectroscopy (Fig. S49). No significant changes in the absorption profiles were observed for any of the complexes upon exposure to a total light dose of 71.4 J cm^{-2}. Therefore, all complexes appeared to be photostable under the tested conditions.

Antibacterial activity

The antibacterial activity of the complexes was evaluated against the Gram-positive *Staphylococcus aureus* and the Gram-negative *Escherichia coli* under both dark and irradiated conditions (Fig. 6a and Table 3). Irradiation was performed in an incubator equipped with an array of fluorescent lamps that covered the visible region from 400 nm to 800 nm (for the full emission spectrum see Fig. S50). **[Ru(DIP)$_2$phen]$^{2+}$** and the free ligands **L-O3** and **L-O4** were utilised as control compounds for this study. Both ligands were found to be inactive against both bacterial strains in the dark and, due to their lack of absorption in the visible region, exhibited an identical lack of activity upon irradiation. Against *E. coli*, all investigated complexes exhibited limited activity. **Ru-DIP-O3** and **Ru-DIP-O4** were the most active derivatives within the series (Fig. S51); however, even these complexes exhibited bacterial inhibition below 50% upon irradiation at the highest tested concentration (100 μM). Consequently, their EC$_{50}$ values are estimated to exceed 100 μM. Regarding *S. aureus*, only the DIP-containing derivatives exhibited pronounced light-driven antibacterial activity (Fig. S52 and S53). In contrast, the bpy analogues showed no significant inhibition of bacterial growth across the tested concentration range, irrespective of irradiation. This indicates that increasing the hydrophilicity of an already

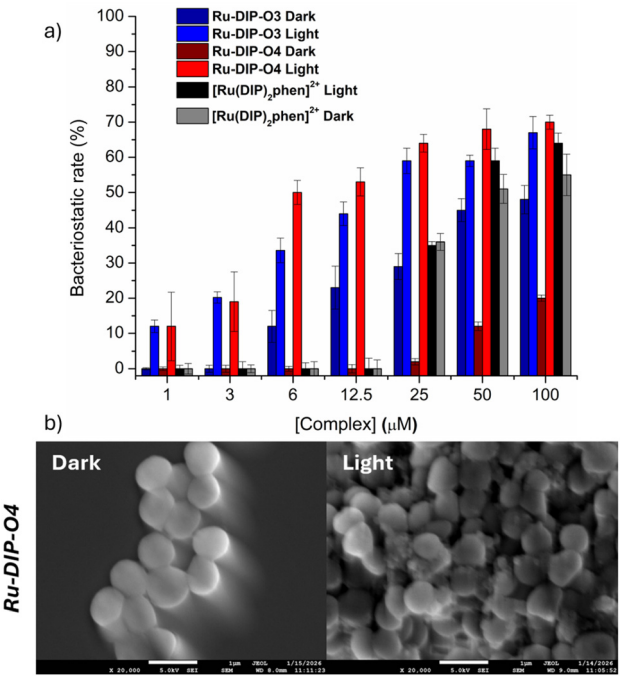

Fig. 6 *In vitro* antibacterial studies. (a) Antibacterial activity of complexes active against *S. aureus* at different concentrations, and (b) SEM images of *S. aureus* cultures treated with **Ru-DIP-O4** in the dark (left) and with irradiation (right).

Table 3 EC_{50} values against *S. aureus* under dark and irradiated conditions

Compound	EC_{50} dark (μM)	EC_{50} light (μM)	PI
Ru-DIP-O3	>100	21.7	>4.6
Ru-DIP-O4	>100	6.0	>16.7
Ru-bpy-O3	>100	>100	—
Ru-bpy-O4	>100	>100	—
$[Ru(DIP)_2phen]^{2+}$	47.7	38.5	1.2

hydrophilic photosensitiser ($[Ru(bpy)_3]^{2+}$, $\log P_{o/w} = -2.00$) resulted in compounds (**Ru-bpy-O3** and **Ru-bpy-O4**) that interact poorly with bacterial membranes. Additionally, **$[Ru(DIP)_2phen]^{2+}$** displayed no significant antibacterial activity at low concentrations (1–12.5 μM), whereas at higher concentrations (>25 μM) the bacteriostaticity increases abruptly. However, due to its high dark toxicity, the complex yields a low photo-index (PI) of 1.2 overall. This concentration-dependent activity for **$[Ru(DIP)_2phen]^{2+}$** correlates with our aggregation studies (*vide supra*), which show that aggregation is observed only at higher concentrations. The increased dark toxicity observed for **$[Ru(DIP)_2phen]^{2+}$** can be attributed to its relatively high lipophilicity, since, as discussed above, excessive lipophilicity has been associated with decreased photodynamic activity and low phototherapeutic indices *in vitro*.[38]

Irradiation of *S. aureus* strains treated with **Ru-DIP-O3** and **Ru-DIP-O4** resulted in an increase in the cytotoxicity of the compounds. More specifically, **Ru-DIP-O3** displayed an EC_{50} value of 21.7 μM, while **Ru-DIP-O4** was markedly more potent, with an EC_{50} of 6.0 μM (Fig. 6a, Fig. S51 and Table 3). The superior performance of **Ru-DIP-O4** is further underscored by its higher PI value in comparison with **Ru-DIP-O3**. At lower concentrations, **Ru-DIP-O4** exhibited minimal to negligible dark toxicity, whereas irradiation led to a substantial enhancement of antibacterial activity, resulting in a PI exceeding 16.7 (Table 3).

The significantly higher phototoxicity of **Ru-DIP-O4** relative to **Ru-DIP-O3** likely stems from differences in their physical behaviour rather than their intrinsic photosensitising efficiency. While both complexes form amphiphilic aggregates, small variations in their mean hydrodynamic diameters and aggregate stability determine their ability to interact with the bacterial envelope. The observed selectivity for Gram-positive *S. aureus* over Gram-negative *E. coli* further supports this hypothesis. Gram-negative bacteria possess an outer membrane that acts as a formidable permeability barrier, likely excluding these aggregates regardless of minor size differences. In contrast, Gram-positive bacteria lack this outer membrane and possess a relatively porous peptidoglycan layer. In this environment, even modest shifts in aggregate size or surface charge can significantly alter how effectively the complex penetrates the cell wall and associates with the cytoplasmic membrane, explaining the pronounced divergence in activity between these two closely related complexes.

Furthermore, these findings are supported by scanning electron microscopy (SEM) analysis of *S. aureus* cultures treated with the complexes at 50 μM (Fig. 6b). For this analysis, based on our *in vitro* cytotoxicity results, we chose to study our most promising complex, **Ru-DIP-O4**, and as controls, **Ru-bpy-O4** that possesses the same ligand (**L-O4**) and **$[Ru(DIP)_2phen]^{2+}$** that is virtually the same complex without the polyether chain. In a similar fashion, two sets of samples were prepared: one maintained under dark conditions and the other subjected to irradiation. Pronounced morphological alterations, consistent with severe membrane disruption, were observed exclusively in cultures treated with **Ru-DIP-O4** upon irradiation. In contrast, cultures treated with the same compound but kept in the dark exhibited no discernible morphological differences relative to the untreated control, validating the high PI value calculated for this compound. Additionally, in the cultures treated with **Ru-bpy-O4** and **$[Ru(DIP)_2phen]^{2+}$** no significant membrane alterations were evident (Fig. S54 and S55).

Conclusions

Here, we present the synthesis and study of the photodynamic antibacterial activity of four new bis-heteroleptic Ru(II) complexes featuring bpy or DIP as ancillary ligands in combination with phenanthroline ligands functionalised with polyether chains of differing lengths to regulate hydrophilicity. The bpy complexes (**Ru-bpy-O3** and **Ru-bpy-O4**) showed clear hydrophilic character, while the DIP complexes (**Ru-DIP-O3** and **Ru-DIP-O4**) exhibited amphiphilic behaviour. Dynamic light scattering studies showed that the amphiphilic DIP complexes form aggregates in aqueous environments, while the bpy analogues remain monomeric under the same conditions. The aggregation mode shown by the DIP complexes, where the Ru(II) core is proposed to be shielded within the aggregate interior while the hydrophilic polyether chains remain solvent-exposed, has not, to the best of our knowledge, been described before and was found to influence both the photophysical properties and the biological activity of the complexes. The aggregated complexes exhibited at least a two-fold increase in their emission lifetimes in comparison with their monomeric forms. We attribute this observation chiefly to the structural rigidification of the Ru(II) polypyridyl chromophores. Importantly, the self-assembly behaviour of the DIP-containing complexes did not compromise their photochemical function, as the complexes retained type I and type II photosensitising activity comparable to **$[Ru(bpy)_3]^{2+}$**, as evidenced from high singlet oxygen quantum yields (Φ_Δ = 0.59–0.64) and robust ROS generation. Antibacterial studies showed that, upon irradiation, **Ru-DIP-O4** significantly inhibits bacterial growth at low micromolar concentrations (EC_{50} = 6.0 μM) while maintaining minimal dark toxicity, corresponding to a photo-index of over 16.7. These findings are corroborated by SEM studies, which revealed that *S. aureus* cultures treated with **Ru-DIP-O4** exhibit significant morphological changes, indicative of membrane disruption, only upon exposure to light.

In conclusion, this work highlights the potential of Ru(II) polypyridyl complexes as photodynamic antimicrobial agents and demonstrates how ligand functionalisation can influence biological performance without sacrificing their inherent photochemical activity. Overall, our findings indicate that alternative design principles can be explored for the development of amphiphilic metal-based photosensitisers and lay the groundwork for future studies aimed at optimising selectivity, understanding uptake mechanisms in greater detail, and expanding the scope of photodynamic antimicrobial therapy.

Experimental section

Materials and methods

Unless otherwise specified, common chemicals and solvents (HPLC grade or reagent grade quality) were purchased from commercial sources and used without further purification.

General synthetic information

Reactions that were not carried out under standard atmospheric conditions were performed under an Ar atmosphere. For reactions that required dry conditions, all glassware was heated to 120 °C for 2 hours and dry solvents were used. The progress of the reactions was monitored using thin-layer chromatography (TLC) using Supelco TLC PET plates coated with silica gel F_{254}. Column chromatography purification was carried out using silica gel 60 (70–230 mesh) or deactivated aluminium oxide (Grade II, 3% H_2O w/w).

The synthesis of compounds 1,10-phenanthroline-5,6-oxide [**1**], 5-hydroxy-1,10-phenanthroline [**2**] and [$Ru(DIP)_2Cl_2$] was adapted from literature procedures.[52,73]

Synthesis of 2-(2-((1,10-phenanthrolin-5-yl)oxy)ethoxy)ethan-1-ol (L-O3). The reaction was carried out under an Ar atmosphere and under dry conditions. Compound **2** (70 mg, 0.35 mmol, 1 eq.), powdered K_2CO_3 (484 mg, 3.5 mmol, 10 eq.) and 2-(2-chloroethoxy)ethanol (41 μL, 0.38 mmol, 1.1 eq.) were added to dry DMF (5 mL). The resulting mixture was then heated to 70 °C and stirred for 12 hours. The progress of the reaction was monitored using TLC analysis (developed with EtOAc/i-PrOH/$NH_{3(aq)}$, 4 : 2 : 1). After the completion of the reaction, DMF was evaporated and the crude product was redissolved in a mixture of DCM/brine and transferred to an extraction funnel. The product was extracted with DCM (3 × 30 mL), dried with $MgSO_4$ and evaporated to dryness. For further purification of the product, column chromatography (silica gel) was performed with DCM/MeOH 95 : 5 as the eluent. The pure product was collected as a white solid (yield: 60%). ^{1}H NMR (500 MHz, chloroform-*d*) δ 9.20 (d, J = 4.3 Hz, 1H), 9.02 (d, J = 4.2 Hz, 1H), 8.70 (d, J = 8.2 Hz, 1H), 8.10 (d, J = 8.1 Hz, 1H), 7.65 (dd, J = 8.2, 4.3 Hz, 1H), 7.56 (dd, J = 8.1, 4.2 Hz, 1H), 6.97 (s, 1H), 4.45–4.41 (m, 2H), 4.08–4.05 (m, 2H), 3.84–3.80 (m, 2H), 3.80–3.75 (m, 2H). ESI-MS theoretical calculation for $[M + H]^+$ = 285.12 – experimental value = 284.85.

Synthesis of 2-(2-(2-((1,10-phenanthrolin-5-yl)oxy)ethoxy)ethoxy)ethan-1-ol (L-O4). The reaction was carried out under an Ar atmosphere and under dry conditions. Compound **2** (80 mg, 0.40 mmol, 1 eq.), powdered K_2CO_3 (552 mg, 4 mmol, 10 eq.) and 2-[2-(2-chloroethoxy)ethoxy]ethanol (118 μL, 0.80 mmol, 2 eq.) were added to dry DMF (5 mL). The resulting mixture was then heated to 80 °C and stirred for 12 hours. The progress of the reaction was monitored using TLC analysis (developed with EtOAc/i-PrOH/$NH_{3(aq)}$, 4 : 2 : 1). After the completion of the reaction, DMF was evaporated and the crude product was redissolved in a mixture of DCM/brine and transferred to an extraction funnel. The product was extracted with DCM (3 × 30 mL), dried with $MgSO_4$ and evaporated to dryness. For further purification of the product, column chromatography (aluminum oxide) was performed with DCM/MeOH (96.5 : 3.5) as the eluent. The product was collected as a clear dark yellow oil (yield, 63%). ^{1}H NMR (600 MHz, chloroform-*d*) δ 9.19 (d, J = 4.3 Hz, 1H), 9.02 (d, J = 4.2 Hz, 1H), 8.72 (d, J = 8.2 Hz, 1H), 8.10 (d, J = 8.1 Hz, 1H), 7.65 (dd, J = 8.2, 4.3 Hz, 1H), 7.56 (dd, J = 8.0, 4.2 Hz, 1H), 6.97 (s, 1H), 4.45–4.42 (m, 2H), 4.08–4.05 (m, 2H), 3.84–3.81 (m, 2H), 3.76–3.72 (m, 4H), 3.65–3.62 (m, 2H). ESI-MS theoretical calculation for $[M + H]^+$ = 329.14 – experimental value = 328.95.

General synthetic procedures of the Ru(II) complexes

A mixture of *cis*-[$Ru(bpy)_2Cl_2$] or *cis*-[$Ru(DIP)_2Cl_2$] and each ligand (**L-O3** or **L-O4**) in 2 mL of EtOH/H_2O (1 : 1) was refluxed for 12 h under an Ar atmosphere and under dark conditions. The mixture gradually turned from dark purple to a deep red solution. Upon completion of the reaction, the reaction mixture was cooled to room temperature, and the solvent was removed under reduced pressure. The crude product was purified *via* flash column chromatography (silica gel) using a gradient of MeCN/$KNO_{3(aq)}$ (0.05 M) (ranging from 12 : 1 to 8 : 1) as the solvent system. The desired fractions were collected, concentrated and redissolved in water containing a small amount of ethanol. To this mixture, a saturated KPF_6 solution was added, and the product was collected by filtration as a PF_6^- salt. The solid was washed with water to remove excess salts and then dried. When required, a portion of the product was converted to its chloride salt *via* an ion exchange column using AmberLite IRA 410 resin.

Synthesis of [$Ru(bpy)_2$(L-O3)]Cl_2 (Ru-bpy-O3). According to the general procedure, *cis*-[$Ru(bpy)_2Cl_2$] (25 mg, 0.051 mmol) and **L-O3** (14.7 mg, 0.051 mmol) were used. **Ru-bpy-O3**$(PF_6)_2$ was obtained as a red solid (41 mg, 0.042 mmol, 82%). ^{1}H NMR (400 MHz, MeOD) δ 8.94 (d, J = 9.6 Hz, 1H), 8.72 (dd, J = 15.2, 8.2 Hz, 4H), 8.54 (d, J = 9.4 Hz, 1H), 8.20–8.12 (m, 3H), 8.06 (t, J = 7.3 Hz, 2H), 7.95 (d, J = 6.3 Hz, 1H), 7.92 (t, J = 5.5 Hz, 2H), 7.82 (dd, J = 8.4, 5.3 Hz, 1H), 7.71 (dd, J = 8.3, 5.2 Hz, 1H), 7.65 (s, 1H), 7.63 (d, J = 5.6 Hz, 2H), 7.56–7.50 (m, 2H), 7.32 (t, J = 8.7 Hz, 2H), 4.61–4.55 (m, 2H), 4.09–4.05 (m, 2H), 3.70 (s, 4H). ^{13}C NMR (101 MHz, MeOD) δ 157.51, 157.26, 154.17, 152.48, 151.64, 151.60, 151.40, 151.37, 149.36, 148.18, 143.65, 137.96, 137.85, 135.63, 132.23, 131.95, 127.60, 127.51, 126.10, 126.03, 125.70, 124.36, 124.33, 124.31, 124.27, 103.35, 72.63, 69.42, 69.02, 60.91. HRMS (ESI) calculated for m/z $[M]^{2+}$ = 349.08; found 349.07.

Synthesis of $[Ru(bpy)_2(L\text{-}O4)]Cl_2$ (Ru-bpy-O4). According to the general procedure, *cis*-$[Ru(bpy)_2Cl_2]$ (25 mg, 0.051 mmol) and **L-O4** (16.7 mg, 0.051 mmol) were used. Due to its high solubility in water, [**Ru-bpy-O4**]$(PF_6)_2$ was not collected by filtration; instead, the solvent was fully evaporated. Next, the complex was re-dissolved in DCM and washed with water to remove excess salts (3 × 10 mL). The organic phase was dried with $MgSO_4$ and filtered and the solvent was removed under reduced pressure, leaving the pure product as a red solid (45 mg, 0.044 mmol, 85%). ^{1}H NMR (400 MHz, MeOD) δ 8.98 (d, J = 9.6 Hz, 1H), 8.76 (dd, J = 15.3, 8.2 Hz, 4H), 8.57 (d, J = 7.3 Hz, 1H), 8.23–8.16 (m, 3H), 8.10 (t, J = 8.4 Hz, 2H), 8.01–7.94 (m, 3H), 7.86 (dd, J = 8.4, 5.3 Hz, 1H), 7.75 (dd, J = 8.3, 5.2 Hz, 1H), 7.69–7.65 (m, 3H), 7.59–7.54 (m, 2H), 7.36 (t, J = 8.1 Hz, 2H), 4.65–4.60 (m, 2H), 4.13–4.08 (m, 2H), 3.87–3.80 (m, 2H), 3.73–3.70 (m, 2H), 3.66–3.62 (m, 2H), 3.61–3.55 (m, 2H). ^{13}C NMR (101 MHz, MeOD) δ 157.51, 157.29, 157.25, 154.14, 152.47, 151.64, 151.59, 151.40, 151.37, 149.36, 148.18, 143.66, 137.95, 137.84, 135.63, 132.22, 131.94, 127.59, 127.51, 126.09, 125.70, 124.34, 124.31, 124.29, 124.25, 103.34, 72.40, 70.58, 70.18, 69.32, 69.07, 60.88. HRMS (ESI) calculated for m/z $[M]^{2+}$ = 371.09; found 371.09.

Synthesis of $[Ru(DIP)_2(L\text{-}O3)]Cl_2$ (Ru-DIP-O3). According to the general procedure, *cis*-$[Ru(DIP)_2Cl_2]$ (25 mg, 0.029 mmol) and **L-O3** (8.5 mg, 0.029 mmol) were used. **Ru-DIP-O3**$(PF_6)_2$ was obtained as a red solid (33 mg, 0.024 mmol, 85%). ^{1}H NMR (400 MHz, MeOD) δ 9.02 (d, J = 7.4 Hz, 1H), 8.62 (d, J = 7.6 Hz, 1H), 8.41–8.35 (m, 3H), 8.33 (s, 4H), 8.28 (dd, J = 5.5, 2.7 Hz, 2H), 8.15 (d, J = 4.3 Hz, 1H), 7.85 (dd, J = 8.4, 5.3 Hz, 1H), 7.80–7.57 (m, 26H), 4.69–4.60 (m, 2H), 4.15–4.10 (m, 2H), 3.75 (s, 4H). ^{13}C NMR (101 MHz, MeOD) δ 154.25, 152.96, 152.22, 152.17, 151.98, 149.84, 149.54, 148.67, 148.63, 148.61, 148.56, 144.05, 135.76, 135.74, 135.65, 132.25, 132.02, 129.72, 129.57, 129.06, 128.97, 126.35, 126.32, 126.14, 126.11, 125.72, 103.38, 72.65, 69.45, 69.05, 60.92. HRMS (ESI) calculated for m/z $[M]^{2+}$ = 525.14; found 525.14.

Synthesis of $[Ru(DIP)_2(L\text{-}O4)]Cl_2$ (Ru-DIP-O4). According to the general procedure, *cis*-$[Ru(DIP)_2Cl_2]$ (25 mg, 0.029 mmol) and **L-O4** (9.8 mg, 0.029 mmol) were used. **Ru-DIP-O4**$(PF_6)_2$ was obtained as a red solid (35 mg, 0.025 mmol, 87%). ^{1}H NMR (400 MHz, MeOD) δ 9.02 (d, J = 7.4 Hz, 1H), 8.62 (d, J = 7.6 Hz, 1H), 8.41–8.35 (m, 3H), 8.33 (s, 4H), 8.28 (dd, J = 5.5, 2.7 Hz, 2H), 8.15 (d, J = 4.3 Hz, 1H), 7.85 (dd, J = 8.4, 5.3 Hz, 1H), 7.80–7.57 (m, 26H), 4.69–4.60 (m, 2H), 4.15–4.10 (m, 2H), 3.75 (s, 4H). ^{13}C NMR (101 MHz, MeOD) δ 154.25, 152.96, 152.22, 152.17, 151.98, 149.84, 149.54, 148.67, 148.63, 148.61, 148.56, 144.05, 135.76, 135.74, 135.65, 132.25, 132.02, 129.72, 129.57, 129.06, 128.97, 126.35, 126.32, 126.14, 126.11, 125.72, 103.38, 72.65, 69.45, 69.05, 60.92. HRMS (ESI) calculated for m/z $[M]^{2+}$ = 525.14; found 525.14.

Nuclear magnetic resonance (NMR) spectroscopy

^{1}H, ^{13}C APT and 2-D correlation spectra were recorded at ambient temperature on either Agilent 500 MHz or Bruker 400-WB 400 MHz spectrometers using deuterated solvents as internal deuterium locks. The residual protic signals of $CDCl_3$, MeCN-d_3, DMSO-d_6 and CD_3OD were used as references in ^{1}H and ^{13}C NMR spectra. Chemical shifts of the protons of the final products were assigned based on COSY and HSQC correlations. The data were analyzed using MestReNova software.

Mass spectrometry

Liquid chromatography-mass spectrometry (LC-MS) analysis was performed on a Thermo Scientific™ Vanquish™ Flex Quaternary UHPLC column C18 type, coupled with a Thermo Scientific LCQ Fleet Ion Trap mass spectrometer with ESI. The compounds were eluted with a gradient of 10% to 90% MeCN/H_2O 0.1% TFA in 12.5 minutes. High resolution mass spectrometry (HRMS) spectra were recorded with a Thermo Finnigan LTQ Orbitrap.

Dynamic light scattering (DLS) studies

The self-assembly of the complexes was investigated *via* DLS analysis. Particle size distribution analysis of the complexes was performed using an Anton Paar Litesizer 500 at 25 °C (light source; 658 nm). Samples were prepared with aqueous solvents filtered with 0.22 μm filters (50 μM).

Lipophilicity assessment

The lipophilicity of the compounds was assessed by determining their log $P_{o/w}$ values using the shake-flask method.[53] Water and n-octanol were stirred overnight at room temperature to ensure saturation of each phase with the other. The two phases were then separated for solution preparation. Each compound was dissolved in the aqueous phase (50 μM, 5 mL) and then the octanol phase (5 mL) was introduced. The mixture was vigorously stirred overnight at room temperature and then left to separate. By measuring the absorbance at 450 nm of each phase separately and using the following equation, the log $P_{o/w}$ values were determined:

$$\log P_{o/w} = \log\left(\frac{A_{450(n\text{-octanol})}}{A_{450(water)}}\right)$$

Photophysical studies

Absorption spectra were measured using a JASCO V-750 UV-vis spectrophotometer. Emission and excitation spectra were recorded on an Edinburgh Instruments FS5 spectrofluorometer equipped with a red-sensitive Hamamatsu R13456 photomultiplier tube (PMT) using a 150 W xenon arc lamp as an excitation source. All spectra were corrected for detector response using the software (Fluoracle) provided by the manufacturer. Emission lifetime measurements were performed using an Edinburgh Instruments mini-τ lifetime spectrometer with a bandpass filter (±40 nm) at 650 nm on the emission side. The excitation source was an Edinburgh Instruments picosecond pulsed LED (EPLED-320) with a peak wavelength of 326.8 nm and a pulse width of 910 ps, and the detector was a thermoelectrically cooled, high-speed red-sensitive photomultiplier tube (Hamamatsu H10720-01). The data were analysed using the software (Fluoracle) provided by the manufacturer.

The molar absorptivity of each complex was calculated from absorbance values according to the Beer–Lambert law in MeCN and Tris–HCl aqueous buffer (0.05 M, pH = 7.4) solutions (50 μM). The luminescence quantum yields of the complexes were measured in MeCN and Tris–HCl buffer, using optically dilute conditions with an air-equilibrated aqueous solution of $[Ru(bpy)_3]Cl_2$ (Φ_{em} = 0.04, λ_{exc} = 436 nm)[65] as the reference. The energies of the emissive states were calculated from the maxima of the highest energy vibronic components observed in the emission spectra (λ_{exc} = 450 nm) recorded at 77 K in a frozen glass matrix (EtOH/MeOH, 4 : 1). Excitation spectra were recorded with a monitoring wavelength of 620 nm. The emission lifetimes were recorded in MeCN and water or aqueous buffers. All the above measurements were carried out on 3 mL quartz cuvettes with a path length of 1 cm, in air-equilibrated samples and, unless otherwise stated, at ambient temperature.

Direct measurement of photoinduced $^1O_2$ generation

The direct measurements of photoinduced $^1O_2$ generation quantum yields in MeCN were performed using a previously reported custom-built setup.[74] The production of $^1O_2$ was evaluated spectroscopically by measuring the phosphorescence signal of the generated $^1O_2$ with a NIR detector at *ca.* 1270 nm. The NIR spectra were acquired from 1100 nm to 1400 nm within 20 seconds at 298 K with an Avantes NIR256-1.7TEC spectrometer. Isoabsorbing samples of the complexes (A = 0.1) were prepared in MeCN and irradiated with a 450 nm laser (80 mW). The $^1O_2$ generation quantum yield (Φ_Δ) values were calculated using $\mathbf{[Ru(bpy)_3]^{2+}}$ as a reference ($\Phi_{\Delta,r}$ = 0.57 in MeCN)[17] and the following equation:

$$\Phi_{\Delta,s} = \Phi_{\Delta,r}\left(\frac{A_{450,r}}{A_{450,s}}\right)\left(\frac{I_s}{I_r}\right)$$

where Φ_Δ is the quantum yield of $^1O_2$ generation, A_{450} is the absorbance at 450 nm, and I is the integrated $^1O_2$ emission intensity, while the "s" and "r" subscripts correspond to the sample and the reference compound, respectively.

Indirect measurement of photoinduced $^1O_2$-ROS generation and photochemical stability

For the indirect ROS generation measurements and photostability assessment, all absorption spectra were recorded on an Agilent Technologies Cary 60 UV-Vis spectrometer equipped with a Cary Single Cell Peltier Accessory for temperature control. The NewEnergy LEDs that were utilized for the irradiation of the systems were purchased from Mouser Electronics and the surface power densities at the irradiation wavelength were measured using an optical Nova Power Meter from Ophir Photonics. The following experiments were performed in duplicate.

The indirect determination of the photoinduced $^1O_2$ generation quantum yield was performed *via* the ABDA (9,10-anthracenediyl-bis(methylene) dimalonic acid) assay. Each solution contained ABDA (100 μM) and the studied compound (25–50 μM, the concentration was adjusted in order for each solution to be iso-absorbing at 450 nm and under 0.1 absorbance) in PBS at 37 °C. Two series of experiments were conducted, one under dark conditions and the other upon irradiation with a blue LED source (450 nm, 19.9 mW cm^{-2}, total light dose = 5.958 J cm^{-2}) placed directly on top of the cuvette while an absorption spectrum was recorded every 60 seconds, for a total of 5 minutes. During both experiments UV-vis spectra were recorded every 10 s and the reduction of the intensity of the characteristic absorption peak of ABDA at 380 nm was plotted against time ($A_o - A_t$ *vs.* t).

As for general ROS photogeneration assessment, mixtures of the dye DHR-123 (10 μM) with each compound (1 μM) were prepared in a PBS buffer (1% DMSO) and then irradiated for 5 min with a blue LED source (450 nm, 20.0 mW cm^{-2}, total light dose = 6.00 J cm^{-2}) as described above. Emission spectra were recorded every minute (λ_{exc} = 500 nm) in the range of 520 to 600 nm to track the enhancement of the emission of DHR-123 (λ_{max} = 528 nm), which is indicative of ROS production.

The photochemical stability of the complexes in water at 37 °C was assessed using UV-vis spectroscopy. Each complex was irradiated for 1 h at 450 nm with a blue LED source (19.9 mW cm^{-2}, total light dose = 71.3 J cm^{-2}) as described above.

Antibacterial photodynamic activity assessment

Escherichia coli and *Staphylococcus aureus* were grown in LB medium for 18–20 hours at 37 °C with shaking (180 rpm). The precultures were transferred into sterile M9 medium and incubated at 37 °C until an optical density of OD_{600} = 0.5–0.6 was reached. The cultures were then diluted with fresh M9 medium to OD_{600} = 0.1.

The antibacterial activity of the complexes was evaluated in sterile 96-well plates, under irradiation as well as under dark conditions. Each plate contained untreated bacterial controls, bacterial cultures treated with test complexes across a concentration range of 1–100 μM, and wells containing the complexes in M9 medium without bacteria for background correction. The remaining wells were filled with sterile M9 or double-distilled water to minimize evaporation effects.

For dark controls, plates were incubated for 12 hours at 37 °C without light exposure. For photodynamic assessment, plates were incubated for 20 minutes after compound treatment to allow sufficient uptake and then irradiated for 10 minutes (using an array of Osram T8 Fluora G13 L 18 W/77 lamps) while being incubated, followed by an additional 12 hours of incubation in the dark. Following incubation, the bacterial growth was quantified by measuring the OD_{600} value of each well. The EC_{50} values were obtained by fitting dose–response curves to the normalized growth data. Finally, the photodynamic activity index (PI = PhotoIndex) was calculated, defined as:

$$PI = \frac{[EC_{50}]_{dark}}{[EC_{50}]_{light}}$$

The optical density of the bacterial cultures was routinely monitored using a Jenway 6305 UV-vis spectrophotometer. Dark incubation of the cultures was carried out in a LABTECH shaking incubator, while irradiation of the plates with simultaneous incubation was performed in a Sartorius Certomat BS-T incubator. Optical density measurements of the 96-well plates were recorded using a BioTek ELx800 Absorbance Microplate Reader. Antibacterial activity was evaluated in three independent biological experiments, with each including four technical replicates per concentration. Data are presented as mean ± standard deviation.

SEM sample preparation of treated bacterial cells

S. aureus was cultured and treated according to the antibacterial photodynamic activity protocol described above using a single concentration (50 μM) in 24-well plates. A circular coverslip was placed in each well prior to incubation to allow bacterial adhesion. After 24 h of incubation, the supernatant was carefully removed, and the wells were washed three times with 1 mL of 1× PBS. Cells attached to the coverslips were chemically fixed by adding 0.5 mL of 2.5% (v/v) glutaraldehyde solution in water and incubating for 20 minutes at room temperature. Following fixation, the samples were gently rinsed with 0.5 mL of distilled water to remove excess fixative. Dehydration was performed through a graded ethanol series by sequential immersion in 70%, 90%, and 100% ethanol for 20–30 minutes at each concentration. After dehydration, the samples were allowed to air-dry overnight at room temperature. The dried specimens were subsequently subjected to SEM analysis, where they underwent standard pre-imaging preparation, including mounting and conductive coating, prior to examination in the scanning electron microscope (FESEM-JSM-7610 FPlus).

Author contributions

A. K. S.: conceptualisation, investigation, data curation, formal analysis, methodology, visualisation, writing – original draft, and writing – review and editing. S. A. T.: conceptualisation, investigation, data curation, formal analysis, methodology, project administration, visualisation, writing – original draft, and writing – review and editing. D. V.: data curation, investigation, and writing – review and editing. E. P.: data curation and investigation. R. P.: data curation, investigation, resources, and writing – review and editing. S. B.: resources and writing – review and editing. T. L.: conceptualisation, investigation, data curation, formal analysis, methodology, project administration, supervision, visualisation, writing – original draft, and writing – review and editing.

Conflicts of interest

The authors declare no conflicts of interest.

Data availability

All data supporting the findings of this study are available within the article and its supplementary information (SI). The SI includes synthetic details, NMR and mass spectra of synthesized compounds, LC-MS analyses, additional UV-vis absorption, emission and excitation spectra, emission decay kinetics, ROS generation assay results, antibacterial photodynamic activity data, and scaning electron microscopy (SEM) images. Supplementary information is available. See DOI: https://doi.org/10.1039/d6dt00689b.

References

1 R. Laxminarayan, A. Duse, C. Wattal, A. K. M. Zaidi, H. F. L. Wertheim, N. Sumpradit, E. Vlieghe, G. L. Hara, I. M. Gould, H. Goossens, C. Greko, A. D. So, M. Bigdeli, G. Tomson, W. Woodhouse, E. Ombaka, A. Q. Peralta, F. N. Qamar, F. Mir, S. Kariuki, Z. A. Bhutta, A. Coates, R. Bergstrom, G. D. Wright, E. D. Brown and O. Cars, *Lancet Infect. Dis.*, 2013, **13**, 1057–1098.

2 C. J. Murray, K. S. Ikuta, F. Sharara, L. Swetschinski, G. Robles Aguilar, A. Gray, C. Han, C. Bisignano, P. Rao, E. Wool, S. C. Johnson, A. J. Browne, M. G. Chipeta, F. Fell, S. Hackett, G. Haines-Woodhouse, B. H. Kashef Hamadani, E. A. P. Kumaran, B. McManigal, R. Agarwal, S. Akech, S. Albertson, J. Amuasi, J. Andrews, A. Aravkin, E. Ashley, F. Bailey, S. Baker, B. Basnyat, A. Bekker, R. Bender, A. Bethou, J. Bielicki, S. Boonkasidecha, J. Bukosia, C. Carvalheiro, C. Castañeda-Orjuela, V. Chansamouth, S. Chaurasia, S. Chiurchiù, F. Chowdhury, A. J. Cook, B. Cooper, T. R. Cressey, E. Criollo-Mora, M. Cunningham, S. Darboe, N. P. J. Day, M. De Luca, K. Dokova, A. Dramowski, S. J. Dunachie, T. Eckmanns, D. Eibach, A. Emami, N. Feasey, N. Fisher-Pearson, K. Forrest, D. Garrett, P. Gastmeier, A. Z. Giref, R. C. Greer, V. Gupta, S. Haller, A. Haselbeck, S. I. Hay, M. Holm, S. Hopkins, K. C. Iregbu, J. Jacobs, D. Jarovsky, F. Javanmardi, M. Khorana, N. Kissoon, E. Kobeissi, T. Kostyanev, F. Krapp, R. Krumkamp, A. Kumar, H. H. Kyu, C. Lim, D. Limmathurotsakul, M. J. Loftus, M. Lunn, J. Ma, N. Mturi, T. Munera-Huertas, P. Musicha, M. M. Mussi-Pinhata, T. Nakamura, R. Nanavati, S. Nangia, P. Newton, C. Ngoun, A. Novotney, D. Nwakanma, C. W. Obiero, A. Olivas-Martinez, P. Olliaro, E. Ooko, E. Ortiz-Brizuela, A. Y. Peleg, C. Perrone, N. Plakkal, A. Ponce-de-Leon, M. Raad, T. Ramdin, A. Riddell, T. Roberts, J. V. Robotham, A. Roca, K. E. Rudd, N. Russell, J. Schnall, J. A. G. Scott, M. Shivamallappa, J. Sifuentes-Osornio, N. Steenkeste, A. J. Stewardson, T. Stoeva, N. Tasak, A. Thaiprakong, G. Thwaites, C. Turner, P. Turner, H. R. van Doorn, S. Velaphi, A. Vongpradith, H. Vu, T. Walsh, S. Waner, T. Wangrangsimakul, T. Wozniak, P. Zheng, B. Sartorius, A. D. Lopez, A. Stergachis, C. Moore, C. Dolecek and M. Naghavi, *Lancet*, 2022, **399**, 629–655.

3 M. A. Webber and L. J. V. Piddock, *J. Antimicrob. Chemother.*, 2003, **51**, 9–11.
4 G. D. Wright, *Adv. Drug Delivery Rev.*, 2005, **57**, 1451–1470.
5 J. M. Munita and C. A. Arias, *Microbiol. Spectr.*, 2016, **4**, VMBF-0016-2015.
6 A. J. Schaenzer and G. D. Wright, *Trends Mol. Med.*, 2020, **26**, 768–782.
7 L. L. Silver, *Clin. Microbiol. Rev.*, 2011, **24**, 71–109.
8 E. D. Brown and G. D. Wright, *Nature*, 2016, **529**, 336–343.
9 M. R. Hamblin and T. Hasan, *Photochem. Photobiol. Sci.*, 2004, **3**, 436–450.
10 F. Baquero and B. R. Levin, *Nat. Rev. Microbiol.*, 2021, **19**, 123–132.
11 T. Maisch, *Photochem. Photobiol. Sci.*, 2015, **14**, 1518–1526.
12 M. Kolarikova, B. Hosikova, H. Dilenko, K. Barton-Tomankova, L. Valkova, R. Bajgar, L. Malina and H. Kolarova, *Med. Res. Rev.*, 2023, **43**, 717–774.
13 A. E. O'Connor, W. M. Gallagher and A. T. Byrne, *Photochem. Photobiol.*, 2009, **85**, 1053–1074.
14 M. Wainwright and K. B. Crossley, *J. Chemother.*, 2002, **14**, 431–443.
15 L. C. C. Lee and K. K. W. Lo, *Small Methods*, 2024, **8**, 2301433.
16 F. Heinemann, J. Karges and G. Gasser, *Acc. Chem. Res.*, 2017, **50**, 2727–2736.
17 A. A. Abdel-Shafi, P. D. Beer, R. J. Mortimer and F. Wilkinson, *Helv. Chim. Acta*, 2001, **84**, 2784–2795.
18 A. P. Castano, T. N. Demidova and M. R. Hamblin, *Photodiagn. Photodyn. Ther.*, 2004, **1**, 279–293.
19 L. M. Lifshits, J. A. Roque, H. D. Cole, R. P. Thummel, C. G. Cameron and S. A. McFarland, *ChemBioChem*, 2020, **21**, 3594–3607.
20 S. J. Steinke, M. N. Dunbar, M. A. Amalfi Suarez and C. Turro, *Inorg. Chem.*, 2024, **63**, 11450–11458.
21 Y. Peng, X. Da, W. Zhou, Y. Xu, X. Liu, X. Wang and Q. Zhou, *Dalton Trans.*, 2024, **53**, 3579–3588.
22 T. Le Gall, G. Lemercier, S. Chevreux, K. S. Tücking, J. Ravel, F. Thétiot, U. Jonas, H. Schönherr and T. Montier, *ChemMedChem*, 2018, **13**, 2229–2239.
23 M. Klausen, M. Ucuncu and M. Bradley, *Molecules*, 2020, **25**, 5239.
24 D. R. Rice, H. Gan and B. D. Smith, *Photochem. Photobiol. Sci.*, 2015, **14**, 1271–1281.
25 R. Dosselli, M. Gobbo, E. Bolognini, S. Campestrini and E. Reddi, *ACS Med. Chem. Lett.*, 2010, **1**, 35–38.
26 M. L. Embleton, S. P. Nair, B. D. Cookson and M. Wilson, *J. Antimicrob. Chemother.*, 2002, **50**, 857–864.
27 L. Holden, C. S. Burke, D. Cullinane and T. E. Keyes, *RSC Chem. Biol.*, 2021, **2**, 1021–1049.
28 Y. Wang, Y.-T. Hu, H.-L. Zhang, Y.-Y. Chen, H.-D. Shi, J.-G. Liu and Q.-L. Zhang, *Dalton Trans.*, 2023, **52**, 8051–8057.
29 S. Pierce, M. P. Jennings, S. A. Juliano and A. M. Angeles-Boza, *Inorg. Chem.*, 2020, **59**, 14866–14870.
30 L. Stevens-Cullinane, T. W. Rees, C. Evans, P.-Y. Ho, M. Kintzel, Y. M. Yip, R. Jia, J. Bailey, E. Clifford, R. Alam, S. Maslen, S. Mouilleron, A. Pasquier, O.-R. Song, S. Warchal, J. Redmond, M. Howell, S. Kjær, M. Skehel, M. M. Müller, E. O. Johnson, M. M. Roessler and J. Hess, *J. Am. Chem. Soc.*, 2025, **147**, 44860–44874.
31 B. A. Thomas-Moore, C. A. del Valle, R. A. Field and M. J. Marín, *Photochem. Photobiol. Sci.*, 2022, **21**, 1111–1131.
32 S. M. Sebastian, D. Nag and A. Galstyan, *ACS Appl. Mater. Interfaces*, 2026, **18**, 8867–8880.
33 C. Yin, Z. Wang, X. Ding, X. Chen, J. Wang, E. Yang, W. Wang, L. L. Martin and D. Sun, *J. Mater. Chem. B*, 2021, **9**, 3808–3825.
34 J. Karges, J. Li, L. Zeng, H. Chao and G. Gasser, *ACS Appl. Mater. Interfaces*, 2020, **12**, 54433–54444.
35 J. Karges, D. Díaz-García, S. Prashar, S. Gómez-Ruiz and G. Gasser, *ACS Appl. Bio. Mater.*, 2021, **4**, 4394–4405.
36 J. Karges, M. Tharaud and G. Gasser, *J. Med. Chem.*, 2021, **64**, 4612–4622.
37 A. Sułek, B. Pucelik, M. Kobielusz, A. Barzowska and J. M. Dąbrowski, *Int. J. Mol. Sci.*, 2020, **21**, 8716.
38 S. Roy, E. Colombo, R. Vinck, C. Mari, R. Rubbiani, M. Patra and G. Gasser, *ChemBioChem*, 2020, **21**, 2966–2973.
39 M. M. S. Lee, E. Y. Yu, D. Yan, J. H. C. Chau, Q. Wu, J. W. Y. Lam, D. Ding, R. T. K. Kwok, D. Wang and B. Z. Tang, *ACS Nano*, 2023, **17**, 17004–17020.
40 Y. Liu, R. Qin, S. A. J. Zaat, E. Breukink and M. Heger, *J. Clin. Transl. Res.*, 2015, **1**, 140–167.
41 A. Guerrero-Martínez, Y. Vida, D. Domínguez-Gutiérrez, R. Q. Albuquerque and L. De Cola, *Inorg. Chem.*, 2008, **47**, 9131–9133.
42 S. Finn, A. Byrne, K. S. Gkika and T. E. Keyes, *Front. Chem.*, 2020, **8**, 638.
43 M. S. De Almeida, E. Susnik, B. Drasler, P. Taladriz-Blanco, A. Petri-Fink and B. Rothen-Rutishauser, *Chem. Soc. Rev.*, 2021, **50**, 5397–5434.
44 Y. Peng, Z. Yang, H. Sun, J. Li, X. Lan and S. Liu, *Nanomedicine*, 2025, **16**, 168–208.
45 P. Xue, J. Wang, X. Han and Y. Wang, *Colloids Surf., B*, 2019, **180**, 202–211.
46 J. Xi and H. Liu, *Adv. Ther.*, 2019, **2**, 1900107.
47 R. Chang, K. Subramanian, M. Wang and T. J. Webster, *ACS Appl. Mater. Interfaces*, 2017, **9**, 22350–22360.
48 Y. Zhang, A. Algburi, N. Wang, V. Kholodovych, D. O. Oh, M. Chikindas and K. E. Uhrich, *Nanomedicine*, 2017, **13**, 343–352.
49 A. Moretti, R. M. Weeks, M. Chikindas and K. E. Uhrich, *Langmuir*, 2019, **35**, 5557–5567.
50 J.-F. Gohy, H. Hofmeier, A. Alexeev and U. S. Schubert, *Macromol. Chem. Phys.*, 2003, **204**, 1524–1530.
51 W. Sun, S. Li, B. Häupler, J. Liu, S. Jin, W. Steffen, U. S. Schubert, H.-J. Butt, X.-J. Liang and S. Wu, *Adv. Mater.*, 2017, **29**, 1603702.
52 R. Caspar, C. Cordier, J. B. Waern, C. Guyard-Duhayon, M. Gruselle, P. Le Floch and H. Amouri, *Inorg. Chem.*, 2006, **45**, 4071–4078.

53 E. Baka, J. E. A. Comer and K. Takács-Novák, *J. Pharm. Biomed. Anal.*, 2008, **46**, 335–341.
54 J. McCain, K. L. Colón, P. C. Barrett, S. M. A. Monro, T. Sainuddin, J. A. Roque III, H. D. Cole, M. Pinto, H. Yin, R. P. Thummel, C. G. Cameron and S. A. McFarland, *Inorg. Chem.*, 2019, **58**, 10778–10790.
55 J. Bowers, M. J. Danks, D. W. Bruce and R. K. Heenan, *Langmuir*, 2002, **19**, 292–298.
56 C. B. Giuliano, N. Cvjetan, J. Ayache and P. Walde, *ChemSystChem*, 2021, **3**, e2000049.
57 L. Maja, K. Željko and P. Mateja, *J. Supercrit. Fluids*, 2020, **165**, 104984.
58 J. Rodriguez-Loya, M. Lerma and J. L. Gardea-Torresdey, *Micromachines*, 2024, **15**, 24.
59 K. L. Elbing and R. Brent, *Curr. Protoc. Mol. Biol.*, 2018, **125**, e83.
60 A. Juris, V. Balzani, F. Barigelletti, S. Campagna, P. Belser and A. von Zelewsky, *Coord. Chem. Rev.*, 1988, **84**, 85–277.
61 F. Camara, J. S. Aguirre-Araque, J. Fortage and M.-N. Collomb, *Sustainable Energy Fuels*, 2024, **8**, 1457–1472.
62 M. A. Chagas and W. R. Rocha, *Chem. Phys. Lett.*, 2014, **612**, 78–83.
63 D. Sorsche, M. A. L. Lima, N. Meitinger, K. Prasad, S. Mandal, K. D. Glusac, S. Rau and A. Pannwitz, *Coord. Chem. Rev.*, 2025, **530**, 216454.
64 J. Issberner, F. Vögtle, L. De Cola and V. Balzani, *Chem Eur. J.*, 1997, **3**, 706–712.
65 K. Suzuki, A. Kobayashi, S. Kaneko, K. Takehira, T. Yoshihara, H. Ishida, Y. Shiina, S. Oishi and S. Tobita, *Phys. Chem. Chem. Phys.*, 2009, **11**, 9850–9860.
66 S. A. Tsoni, T. Kench, R. Vilar and T. Lazarides, *Inorg. Chem.*, 2025, **64**, 22340–22354.
67 C. Draeger, C. Böttcher, C. Messerschmidt, A. Schulz, L. Ruhlmann, U. Siggel and and J.-H. Fuhrhop, *Langmuir*, 2000, **16**, 2068–2077.
68 H. Song, A. Amati, A. Pannwitz, S. Bonnet and L. Hammarström, *J. Am. Chem. Soc.*, 2022, **144**, 19353–19364.
69 C. Schweitzer and R. Schmidt, *Chem. Rev.*, 2003, **103**, 1685–1757.
70 T. Entradas, S. Waldron and M. Volk, *J. Photochem. Photobiol. B.*, 2020, **204**, 111787.
71 N. A. Kuznetsova, N. S. Gretsova, O. A. Yuzhakova, V. M. Negrimovskii, O. L. Kaliya and E. A. Luk'yanets, *Russ. J. Gen. Chem.*, 2001, **71**, 36–41.
72 Y. Qin, M. Lu and X. Gong, *Cell Biol. Int.*, 2008, **32**, 224–228.
73 Y. Shen and B. P. Sullivan, *Inorg. Chem.*, 1995, **34**, 6235–6236.
74 M. S. Meijer and S. Bonnet, *Inorg. Chem.*, 2019, **58**, 11689–11698.